



Electron microscopy investigations of changes in morphology and conductivity of LiFePO₄/C electrodes

Scipioni, Roberto; Jørgensen, Peter S.; Ngo, Duc-The; Simonsen, Søren Bredmose; Liu, Zhao; Yakal-Kremski, Kyle J.; Wang, Hongqian; Hjelm, Johan; Norby, Poul; Barnett, Scott A.

Total number of authors:

11

Published in:

Journal of Power Sources

Link to article, DOI:

[10.1016/j.jpowsour.2015.12.119](https://doi.org/10.1016/j.jpowsour.2015.12.119)

Publication date:

2016

Document Version

Publisher's PDF, also known as Version of record

[Link back to DTU Orbit](#)

Citation (APA):

Scipioni, R., Jørgensen, P. S., Ngo, D-T., Simonsen, S. B., Liu, Z., Yakal-Kremski, K. J., Wang, H., Hjelm, J., Norby, P., Barnett, S. A., & Jensen, S. H. (2016). Electron microscopy investigations of changes in morphology and conductivity of LiFePO₄/C electrodes. *Journal of Power Sources*, 307, 259-269.
<https://doi.org/10.1016/j.jpowsour.2015.12.119>

General rights

Copyright and moral rights for the publications made accessible in the public portal are retained by the authors and/or other copyright owners and it is a condition of accessing publications that users recognise and abide by the legal requirements associated with these rights.

- Users may download and print one copy of any publication from the public portal for the purpose of private study or research.
- You may not further distribute the material or use it for any profit-making activity or commercial gain
- You may freely distribute the URL identifying the publication in the public portal

If you believe that this document breaches copyright please contact us providing details, and we will remove access to the work immediately and investigate your claim.



Electron microscopy investigations of changes in morphology and conductivity of LiFePO₄/C electrodes

Roberto Scipioni ^{a,*}, Peter S. Jørgensen ^a, Duc-The Ngo ^{a,c}, Søren B. Simonsen ^a, Zhao Liu ^b, Kyle J. Yakal-Kremski ^b, Hongqian Wang ^b, Johan Hjelm ^a, Poul Norby ^a, Scott A. Barnett ^b, Søren H. Jensen ^a

^a Department of Energy Conversion and Storage, Technical University of Denmark, DTU Risø Campus, Frederiksbergvej 399, 4000 Roskilde, Denmark

^b Department of Material Science and Engineering, Northwestern University, 2220 Campus Drive, Evanston, IL 60208, USA

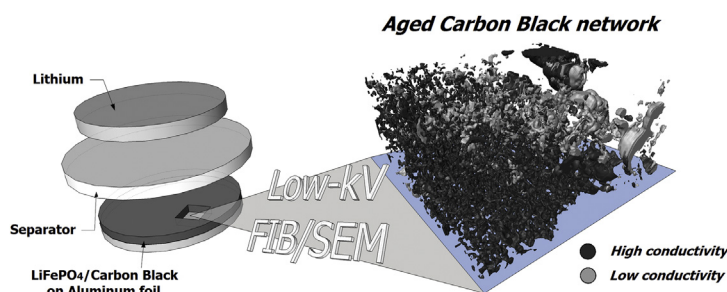
^c School of Materials, The University of Manchester, Oxford Road, Manchester M13 9PL, United Kingdom



HIGHLIGHTS

- Low-kV FIB/SEM is used for first time to analyze degraded LiFePO₄/C cathode.
- Contrast difference allow identification of low-conductive carbon at low-kV.
- LiFePO₄ cracking and carbon agglomeration observed by conventional FIB/SEM.

GRAPHICAL ABSTRACT



ARTICLE INFO

Article history:

Received 7 September 2015

Received in revised form

24 November 2015

Accepted 23 December 2015

Available online xxx

Keywords:

Low accelerating voltage
Focused ion beam scanning electron microscopy
Three-dimensional analysis of LiFePO₄/
Carbon electrode
Degradation mechanism
Loss in electron percolation

ABSTRACT

In this work we study the structural degradation of a laboratory Li-ion battery LiFePO₄/Carbon Black (LFP/CB) cathode by various electron microscopy techniques including low kV Focused Ion Beam (FIB)/Scanning Electron Microscopy (SEM) 3D tomography. Several changes are observed in FIB/SEM images of fresh and degraded cathodes, including cracks in the LFP particles, secondary disconnected particles, and agglomeration of CB. Low voltage (1 kV) SEM images show that the CB agglomerates have a different brightness than the fresh CB, due to charging effects. This suggests that the electronic conductivity of the CB agglomerates is low compared to that of the fresh CB particles. HRTEM analysis shows that fresh CB particles are quasi crystalline, whereas the LFP/CB interface in the degraded electrode shows amorphous carbon surrounding the LFP particles. The presence of the amorphous carbon is known to impede the electronic conductivity and thereby decreasing percolation in the cathode and reducing the electrode capacity.

© 2016 The Authors. Published by Elsevier B.V. This is an open access article under the CC BY license (<http://creativecommons.org/licenses/by/4.0/>).

1. Introduction

Lithium-ion batteries find widespread use in many electricity storage applications, from portable devices to electric vehicles (EV), because of their high energy density and design flexibility [1–3].

* Corresponding author.

E-mail address: roscip@dtu.dk (R. Scipioni).

However, limited lifetime is still a challenge for several Lithium-ion battery materials. To understand the degradation mechanisms and increase the performance of these materials, the development of improved characterization methods is crucial.

LiFePO_4 (LFP) is an interesting material for lithium-ion battery porous cathodes because of its long durability and inherent safety [4,5]. Since LFP is a poor ion and electron conductor, it is usually mixed with carbon black (CB) additives to increase electronic percolation in the electrode. It is well known that mechanical stress related to expansion/contraction of the LFP particles during charging/discharging cycles leads to the formation of micro-cracks inside the LFP particles [6–8], so electronic conductivity and homogeneous dispersion of CB play an important role for long term performance and durability [9,10]. The formation of cracks in the LFP grains leads to disconnected secondary particles, resulting in an increased ionic resistivity and a capacity drop of the electrode. Agglomeration of the CB particles decreases electronic percolation, i.e. increasing the electric resistivity in the CB network from the current collector to the LFP particles [10].

Techniques that can directly quantitatively observe the morphology and structure of the CB phase are limited, however. FIB/SEM tomography has been successfully used to quantify the 3D microstructure of porous electrodes [11–15], and to observe changes in porosity, crack formation, and grain agglomeration [16,17] but, to our best knowledge, no one have used low-kV FIB/SEM tomography to study electron percolation in CB phase. Thydén et al. showed that low-kV SEM imaging is an excellent technique on conventional polished cross-sections for studying electron percolation in the Ni-network in solid oxide fuel cells (SOFC) [18] but it has never been combined with a FIB to study three-dimensionally the electron percolation.

In this work, the degradation of a laboratory-made LFP/CB porous cathode is studied using various electron microscope techniques, including low-kV FIB/SEM tomography. The low-voltage percolation contrast technique shows that the CB agglomerates have lower electronic conductivity in the bulk than that of the fresh CB particles. HRTEM analysis of the LFP/CB interface indicates that the CB agglomerates are amorphous, in contrast to fresh CB particles which are quasi-crystalline. This explains the low CB agglomerate bulk electronic conductivity [19,20].

2. Methods and materials

2.1. Electrode fabrication and test conditions

Slurry was made of commercial LiFePO_4 powder (already carbon coated, from MTI), Super C65 carbon black (from Timcal) and Polyvinylidene Fluoride (PVdF) as binder, with the ratio 80:10:10. From this slurry the electrode material was prepared by casting on aluminum foil. After drying, the thickness was approximately 22 μm thick and two electrodes with a diameter of 18 mm were punched out. The two electrodes were tested in an EL-CELL® ECC-Combi 3-electrode setup, using lithium metal foils counter electrodes, lithium metal as reference electrode and a glass fiber separator soaked with a standard 1 M LiPF_6 in 1:1 EC/DMC electrolyte. Both cells were cycled at constant C-rate using a Biologic VMP3 with Pstat/Gstat boards. Table 1 shows the test conditions for

Table 1

Test conditions for the examined laboratory LFP electrodes.

Electrode	Current (mA g^{-1})	Total cycle number	Remaining capacity
Fresh	17	2	-100%
Aged	17	100	-30%

the two electrodes.

The first electrode, denoted "Fresh", was cycled just two times while the second one, denoted "Aged", was cycled 100 times. Both cells were cycled between 3 and 4 V at a constant current of 17 mA g^{-1} , corresponding to approximately 0.1 C-rate for the fresh electrode. Both electrodes were left in the discharged state before being de-assembled for microscopy analysis.

2.2. FIB/SEM microscopy

FIB tomography and SEM imaging was carried out on a Zeiss 1540XB CrossBeam microscope, using a lateral E-T (Everhart-Thornley) detector and an In-lens detector. Two 3D datasets were collected from the fresh electrode (labeled as F1 and F2) and three from the aged one (labeled as A1, A2 and A3). Conventional SEM imaging has been also performed in another region of the aged sample (A4). Table 2 shows the volume sizes of the 5 different 3D datasets. A Gallium FIB slicing probe of 2 nA was used and the thickness of each slice was estimated to be 40 nm. The serial sectioning imaging was performed at 1 kV with a pixel size of $15 \times 15 \text{ nm}^2$, i.e. the voxel size in the 5 3D-data sets was $40 \times 15 \times 15 \text{ nm}^3$. Conventional SEM imaging was performed at 10 kV, with a pixel size of $15 \times 15 \text{ nm}^2$. The electrodes were prepared for the FIB tomography by rinsing with diethyl carbonate and vacuum infiltrated with a silicon resin (Wacker Chemie) for 30 min to improve phase contrast between CB particles and pores as described by Ender et al. [13]. Subsequently the sample was infiltrated with epoxy resin to enable high-quality grinding and polishing of the sample.

2.3. Low-voltage percolation contrast

Thydén et al. [18] previously used low-voltage SEM imaging to identify percolation in SOFC anode Ni-network. Here we briefly describe the theory behind the percolation contrast.

As the electron beam hit the specimen, a variety of elastic and inelastic scattering of the electrons in the specimen occurs. The elastic and inelastic scattered electrons produce respectively backscattered and secondary electrons (BSE and SE). SEs have by definition energies <50 eV. BSEs have energies close to the acceleration voltage (in our case 1 kV). The SE signal is typically divided into three different kinds of secondary electrons [18,21,22]:

1. SE_1 , generated by interaction of the primary electron beam with the specimen.
2. SE_2 , generated by outgoing BSE.
3. SE_3 , generated by the interaction of BSEs with the internal components of the chamber.

The In-lens detector, situated in the electron column, detects low energy electrons very efficiently due to the beambooster of the GEMINI column (Carl Zeiss, Germany) [23]. This means that the In-lens detector signal contains a high fraction of SE_1 and SE_2 electrons. At the same time the In-lens detector acts as a low energy filter for the E-T detector such that it primarily detects higher

Table 2

Volumes of collected datasets.

Dataset	Volume (voxels) $X \times Y \times Z$	Volume (μm^3) $X \times Y \times Z$
F1	$250 \times 683 \times 341$	$10 \times 10 \times 5$
F2	$141 \times 683 \times 341$	$5.6 \times 10 \times 5$
A1	$250 \times 683 \times 341$	$10 \times 10 \times 5$
A2	$131 \times 683 \times 341$	$5.2 \times 10 \times 5$
A3	$150 \times 683 \times 341$	$6 \times 10 \times 5$

energy electrons (>40 eV) [24].

The interaction volume decreases with the electron acceleration voltage. The visualization of electron percolation in materials is possible at low-kV due to the smaller interaction volume. At higher accelerating voltages the penetration depth of the primary beam is significantly larger (2–3 μm at 10 kV and 20–40 nm at 1 kV). For this reason observation of local small-feature charge phenomena is only possible at a low (~1 kV) acceleration voltage.

Fig. 1a shows a general trend of how the SE yield varies in the low-voltage range for a number of materials comparable to the Si-resin [25,26]. For beam energies higher than E_2 and lower than E_1 (the crossover voltages) less than 1 secondary electron is generated per incident electron. For beam energies between E_1 and E_2 more than 1 secondary electron is generated per incident electron. If the total electron yield (SE and BSE) differs from 1 a surplus or deficit of electrons will build up locally in the specimen. For many polymers E_1 is usually equal to or lower than 0.1 kV, while E_2 is in the range 0.6–1.5 kV, and δ_{\max} is between 2 and 4 [23,27]. **Fig. 1b** presents carbon SE yield data compiled from data presented by D.C. Joy [28]. The SE yield curves follow the same general trend as observed for polymers [25,26] as depicted in **Fig. 1a**. Based on **Fig. 1b**, unfortunately it cannot be concluded whether the yield is higher or lower than 1 at 1 kV based on the presented knowledge for Carbon SE and BSE coefficients. From **Fig. 1a** Si-resin is expected to charge positively.

BSE coefficient for carbon is reported to be quite low, varying between 0.05 and 0.15 [28]. Additionally, a Monte Carlo simulation performed with Casino [29] software indicates that the BSE coefficient for Carbon is 0.06–0.11. BSE values for silicon resin have not been found in literature but a Monte Carlo simulation [29] indicates that they are in the range 0.1–0.12. According to these values, the SE coefficient contributes the most to the total electron yield.

For electron conducting phases with a connection to ground the local buildup of charge is rapidly equalized and no charging effects will occur. For insulators, the lack of charge dissipation means that balancing of the ingoing and outgoing electrons will occur mainly through charging of the particles which changes the secondary electron yield:

- Total electron yield >1: the sample will charge positively. Emission of low energy electrons will be impeded to balance the yield.
- Total electron yield <1: the sample will charge negatively. Deceleration or deflection of the incident beam and emission of additional low energy electrons will balance the yield.

To sum up sufficiently accurate yield-coefficient-values at 1 kV for the carbon black are not readily available and the best indication of the charging regime (positive, negative or not charging) for the

two phases of carbon (non-electron-dissipating and electron-dissipating) is thus to observe their characteristic intensities. As mentioned, the silicon resin used to infiltrate the specimens has a total electron yield higher than 1, meaning that it is expected to charge positively and appear bright, when imaged at 1 kV.

As described above, the result of beam induced charging in an insulator will primarily change the yield of the lowest energy electrons. The contrast changes due to charging are thus almost exclusively seen in the In-lens detector images and the E-T detector images are largely unaffected. It is important to note that this technique only allows us to determine relative differences in the yield and conductivity of each phase; it does not allow a direct quantification of the conductivity.

2.4. Image processing

Segmentation of the 3D FIB/SEM image data was performed with the program ImageJ (NIH). Because of uneven illumination, setting a single threshold for entire micrographs was not feasible. Therefore the Sauvola algorithm [30,31] was so used to perform local thresholds of the data. The Sauvola algorithm works by dividing the input image into square windows ($n \times n$ pixel) and setting thresholds for each of them based on the mean and standard deviation of the pixel intensities. Visualizations of the 3D reconstructions of the analyzed data were performed with the program Avizo (FEI).

The particle size distributions (PSD) of LFP and CB phases in both fresh and aged samples were analyzed based on the method introduced by Münch et al. [32]: The segmented 3D volumes are filled with spheres of a given radius. By reducing the radius incrementally, more volumes will be filled. The cumulative PSD is then obtained by correlating the incrementally filled volume with corresponding radii.

2.5. Transmission electron microscopy

TEM specimen of the fresh sample was prepared by dropping a small drop of cathode solution on an Au TEM grid supported with a holey carbon film, and naturally drying at 120 °C in the air. TEM specimen of the age sample cured in Si resin was prepared by FIB. Transmission electron microscopy (TEM) characterizations (including HRTEM, STEM and X-ray spectroscopy analysis) were conducted on a JEOL JEM 3000F equipped with a 300 kV field emission gun (FEG), high annular angle dark field (HAADF) STEM detector, and an Oxford Instruments X-ray detector with an ultra-thin window for EDX analysis.

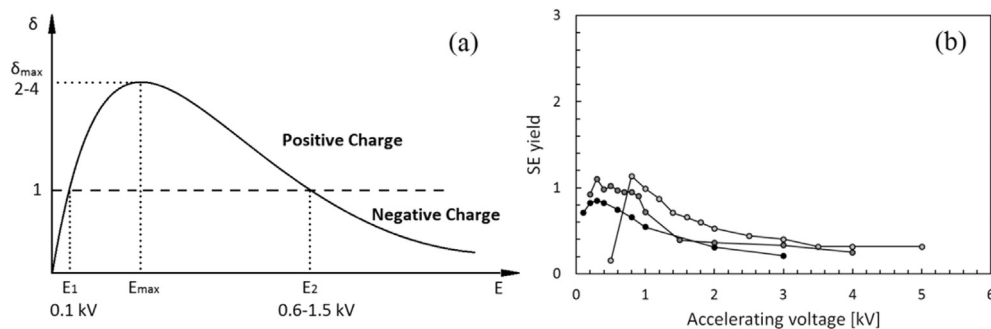


Fig. 1. a) General SE yield curve in the low-voltage range and b) SE yield for carbon according to data compiled by D.C. Joy [28].

3. Results

3.1. SEM images

Fig. 2 shows SEM images after FIB slicing recorded at 1 kV of the fresh electrode (region F1, **Fig. 2 a,b**) and aged electrode (region A1, **Fig. 2 c,d**), and recorded at 10 kV of the aged electrode (region A4, **Fig. 2 e,f**). The images were recorded with the E-T detector (**Fig. 2 a,c,e**) and with the In-lens detector (**Fig. 2 b,d,f**).

In the images recorded at 1 kV with the E-T detector (**Fig. 2 a,c**) it is possible to distinguish three different phases: the grains with the brightest contrast correspond to LFP particles, the almost black regions correspond to CB and the large gray areas in-between correspond to pores filled with silicon resin. The fresh electrode (**Fig. 2a**) shows a relatively homogeneous distribution of sub-micrometer LFP grains and CB particles. On the contrary, the aged sample (**Fig. 2c**) has a less homogeneous distribution of both LFP and CB and an increased porosity. The aged sample is further characterized by the presence of larger CB agglomerates surrounding some LFP grains, which is not observed in the two images

of the fresh electrode. The increased agglomeration is expected to result in a decrease in the percolation of the CB network [9,10].

In the images recorded at 1 kV with the In-lens detector it can further be observed that the silicon resin has high intensity in the parts of the sample not adjacent to electron conducting phases (**Fig. 2b**). The two detectors give different type of contrast and sensitivity to charging, as discussed in the theory section. This indicates that the silicon resin is charging negatively due to low conductivity to the ground [23]. It is expected that the CB network has a good conductivity and connectivity to ground. Consistent with this expectation, the CB in the fresh sample has a dark contrast, which indicates minimal charging (**Fig. 2b**). However, in the aged electrode on (**Fig. 2d**) large agglomerations (circled in red) of what appears to be CB are brighter than other CB regions. This indicates that those agglomerations are charging negatively i.e. have lost connection to ground and/or have low conductivity.

Furthermore, a transition layer (pointed out by green arrows) with intermediate intensity between the CB agglomerates and the silicon resin is also observed as rims around the CB agglomerates in **Fig. 2d**. This indicates a transition zone where the silicon is able to

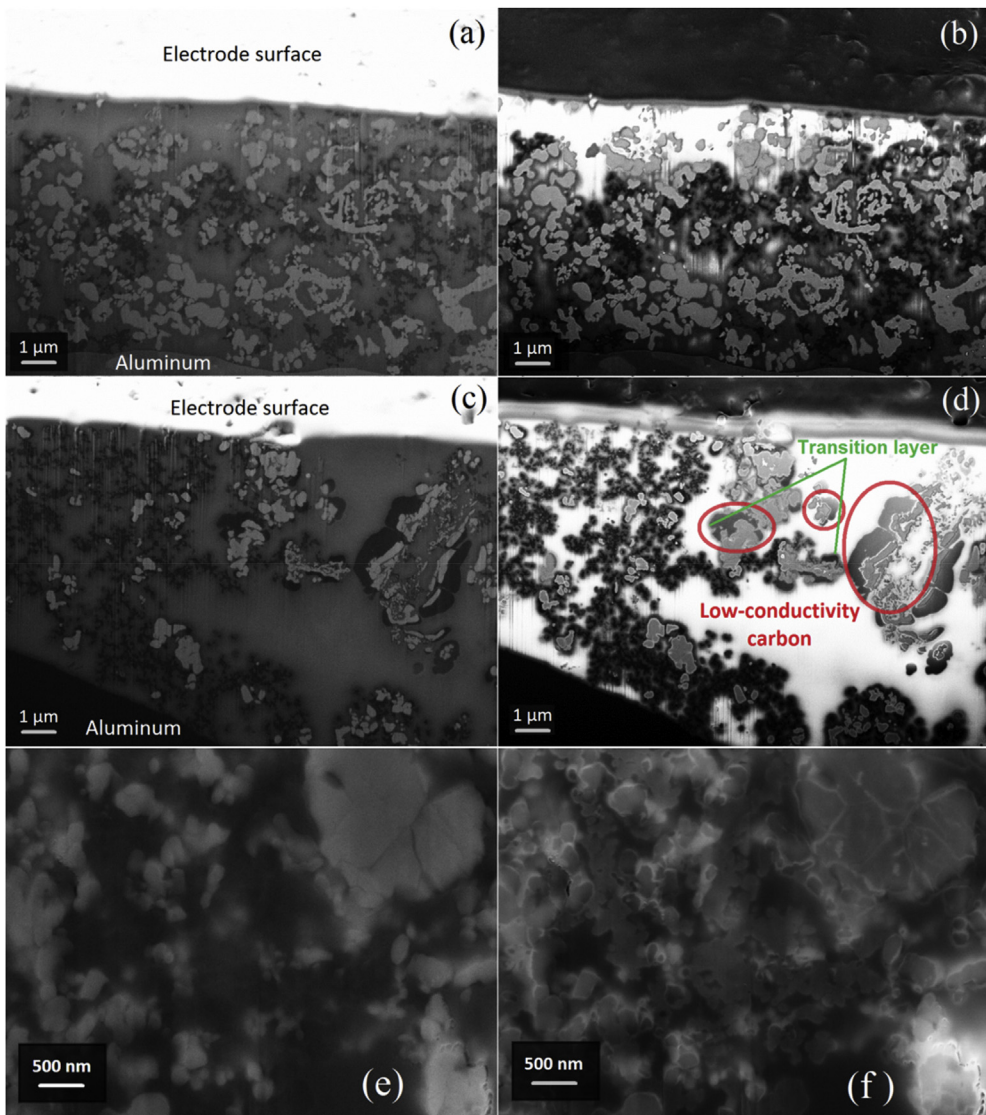


Fig. 2. SEM images at 1 kV of the (a–b) fresh and (c–d) aged electrode recorded with the (a,c) Lateral E-T and (b,d) In-lens detector. SEM images at 10 kV of the (e–f) aged electrode (A4) recorded with the (e) lateral E-T and (f) In-lens detector.

dissipate charge to the CB phase. In the images recorded with the In-lens detector, the LFP particle has a brighter contrast than the CB, which, as one would expect, indicate low electronic conductivity of the LFP particles.

Fig. 2 (e,f) shows SEM images of the aged electrode, at higher magnification recorded at 10 kV. With the relatively high energy of 10 kV, the electrons penetrate app. 2–3 μm into the sample surface and the images therefore give insight into the internal structure of the particles.

SEM images at 10 kV show cracks in some of the LFP grains in area (A4) of the aged electrode (e.g. the large grain in the top right corner of **Fig. 2e**). The cracks are expected to be caused by expansion/contraction of the particle during the lithiation/delithiation process. In the In-lens detector image (**Fig. 2f**) many of the cracks appear as bright highlights due to the easier escape path of secondary electrons at topological LFP edges through the epoxy.

3.2. FIB tomography

The SEM images from the five datasets F1, F2, A1, A2 and A3 are used for three-dimensional reconstructions. **Fig. 3** shows the 3D FIB tomography reconstruction after image segmentation of the 1 kV Lateral E-T image dataset from the fresh (F1) and aged (A1) electrodes, respectively. LFP grains are represented as gray, CB as black, while pores are shown as transparent. From the figure it can be observed again that compared to F1, all phases are less homogeneously distributed in A1. Further, the presence of large CB agglomerates are seen in A1.

From the segmentation of the 3D datasets presented in **Fig. 3** it is possible to extract and calculate statistical data. **Table 3** shows calculated phase fractions for all the analyzed volumes. Relative to the fresh electrode, the aged electrode is characterized by a larger variation in the volume fraction of pores and of CB. This is in agreement with the 2D SEM analysis, where the aged sample was observed to be less homogeneous (**Fig. 2**).

Particle size distribution (PSD) for the LFP phase in the five 3D dataset is presented in **Fig. 4**. It shows a slight shift towards smaller grains in the aged samples compared to the fresh ones and this could be explained by cracking of the particles. The PSD of CB has not been calculated because of the size of the majority of the CB particles is below or comparable to the slicing resolution (~40 nm), which results in considerable uncertainty in determining the particle size.

From the segmented 3D datasets it is also possible to analyze the CB connectivity. In this analysis, a CB voxel is considered connected when it has a pathway to the bottom side of the reconstructed data cube (the direction of the aluminum current collector) through the carbon network. Unknown connectivity is defined as only being connected to one of the other sides of the reconstructed data cube.

Fig. 5 shows the analysis of connected CB in the five 3D data sets. Statistical results of the connectivity analysis are reported in **Table 4**. Both for F1 and F2, the CB networks are highly (97%) connected to the aluminum current collector. Regions from the three aged sample are instead characterized by large variations in connected and isolated fractions. Note that the precision of the connectivity analysis is also affected by the slicing resolution which is not included in the uncertainties given in **Table 4**.

3.3. Charge contrast FIB tomography

As presented in **Fig. 2b** and d, CB with two different contrast levels, apparently revealing the electronically percolated and non-percolated CB, can be obtained when recording the SEM images using an acceleration energy of 1 kV in combination with the in-lens detector. To analyze the two types of CB in 3D, the 1 kV in-

lens SEM images were used for an additional segmentation. **Fig. 6a** shows a 3D reconstruction of the CB network in A1. The black particles represent the apparently electronically percolated CB, while the gray ones show the apparently insulated CB agglomerates.

However, the assumption that the CB agglomerate brightness correlates with electronic percolation seem to be problematic. **Fig. 6** (b, c) show a zoom on a sub-volume and **Fig. 6** (d) show the corresponding raw images.¹ From the inspection of the raw images in the 3D data (**Fig. 6d**), the CB agglomerate brightness is seen to flicker between the grounded intensity level and the insulated (charged) intensity level. The flickering rules out that the increased intensity is due to the entire CB agglomerate being conducting and disconnected from ground. Further, the CB agglomerates appear dark (slices 114 and 116, **Fig. 6d**) where it has a surface connection (in the slicing plane) to grounded CB particles. Additionally, if the CB agglomeration is isolated in the slicing plane the CB agglomeration appears bright (slices 110 and 120). Such intensity flicker was observed to be a general behavior of the examined CB agglomerates. For this reason, we propose that the intensity flipping is attributed to the buildup of electrons on the CB agglomerate/vacuum interface resulting in a brighter contrast, and discharge across the slicing plane surface when adjacent to grounded CB, resulting in the darker contrast. Importantly, and as mentioned above, if the CB agglomerates had sufficient electronic conductivity to dissipate the charge the intensity would not flip from bright to dark on subsequent images. This leads us to suggest that these large CB agglomerations have lower bulk electron conduction. However, the CB agglomerate/vacuum interface seems to be sufficiently conducting to dissipate the SE electrons.

As described above, the apparent percolated and non-percolated CB should rather be interpreted as CB agglomerates with low bulk electric conductivity as opposed to the fresh CB particles with high bulk conductivity. **Table 5** shows the ratio of observed high- and low-conductivity CB for all the analyzed regions. Note that due to the surface discharge of the low-conductivity CB, a part of the low-conductivity CB has a low intensity and is thus not interpreted as low-conductivity CB. For this reason the actual amount of CB with low conductivity might be higher than the observed amount and correspondingly the amount of CB with high electronic conductivity might be lower than the observed amount. No attempts were made to quantify the amount surface-connected low-conductivity CB which could have quantified the difference between the observed and the actual amount of low-conductivity CB.

Supplementary data related to this article can be found online at <http://dx.doi.org/10.1016/j.jpowsour.2015.12.119>.

3.4. TEM images

Fig. 7a show a TEM image of fresh CB where it can be seen that the primary particles have an almost spherical shape with an average diameter of ~40 nm. The selected area electron diffraction (SAED) pattern in the inset of **Fig. 7a** reveals a quasi-crystal structure of CB nanoparticles and from **Fig. 7b** the graphitic sheets oriented concentrically approximately tangent to the CB surface is observed. The distance to the brightest ring in the SAED pattern in **Fig. 7a** is 2.95 nm^{-1} corresponding to (002) planes with a spacing of 0.34 nm. From Fourier transforms of HRTEM images like the one presented in **Fig. 7b**, the mean distance between the graphitic

¹ Additional parts of the raw images, not used for 3D reconstruction, are also shown in the raw images. Further, the raw images also contain the LFP phase which is not shown in the 3D reconstruction of the CB network.

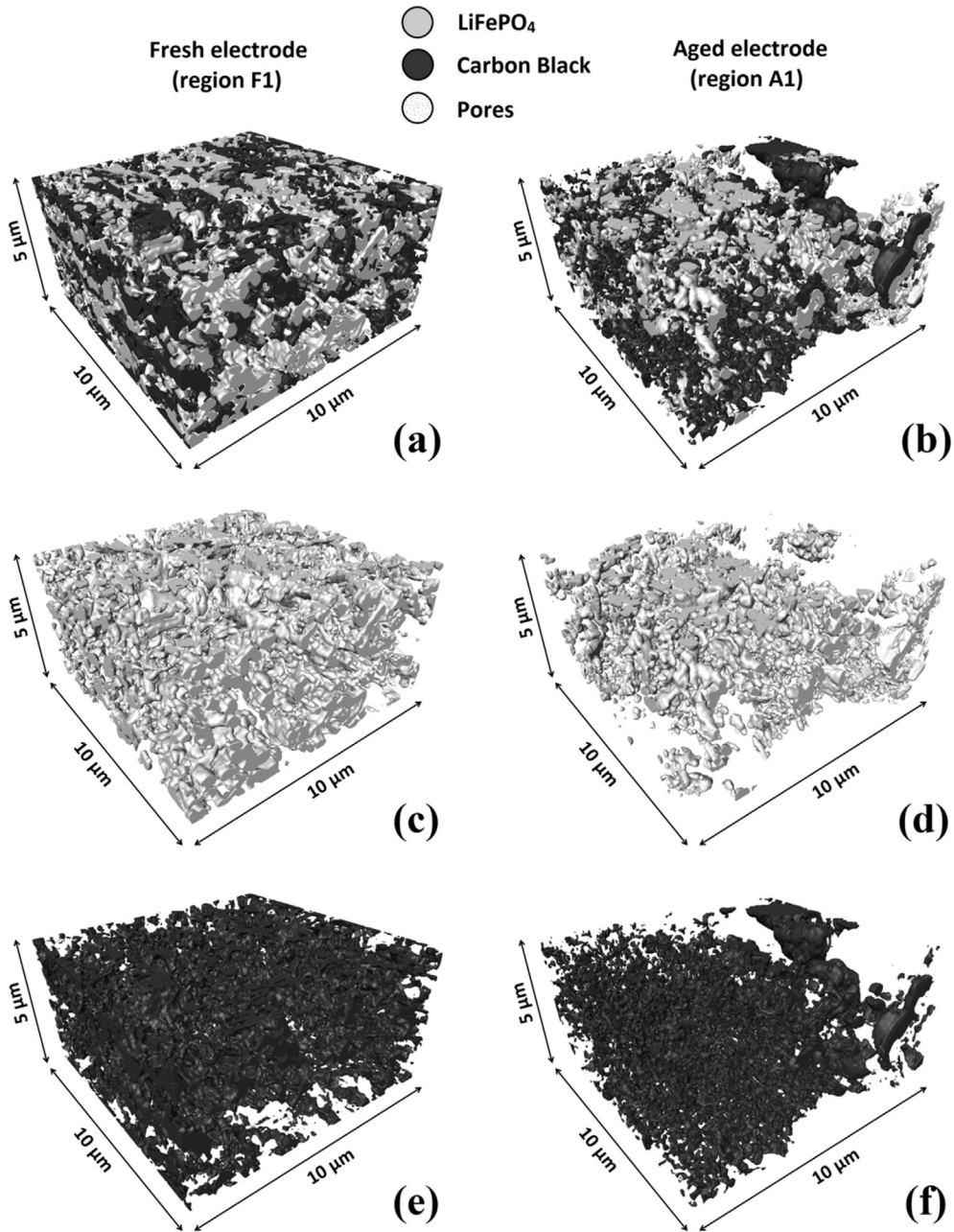


Fig. 3. A segmentation of the 3D FIB tomography reconstruction of a) the fresh (F1) and b) aged (A1) electrode. (c, d) show only the LFP phase and (e, f) show only the CB phase of (F1) and (A1), respectively.

Table 3

Phase volume fraction for fresh and aged electrode.

Phase	F1	F2	Fresh (av. and deviation)	A1	A2	A3	Aged (av. and deviation)
LiFePO ₄	23%	17%	20% ± 3%	12%	18%	12%	14% ± 3%
CB	16%	15%	15.5% ± 0.5%	16%	5%	26%	16% ± 9%
Pores	61%	68%	64.5% ± 3.5%	72%	77%	62%	70% ± 6%

sheets is determined to 0.34 nm consistent with the characteristic distance of the CB (002) planes calculated from the SAED data.

The morphology of the pristine LiFePO₄ nanoparticles can be seen in the TEM images shown in Fig. 7 (c,d). LFP nanoparticles with a size of 200–300 nm are visible in a TEM image in Fig. 7c. Fig. 7d shows a close-up of a typical LFP particle with a lattice spacing of

0.37 nm corresponding to the (011) lattice distance of orthorhombic LiFePO₄. The carbon coating prepared by the commercial supplier is observed as a thin amorphous layer (~2 nm) at the edge.

HRTEM analysis has also been performed on a FIB lamellar specimen of the aged cathode. Fig. 8 shows TEM (a,b) and HRTEM (c,d) images of the LFP/CB aged cathode. A bright-contrast layer is

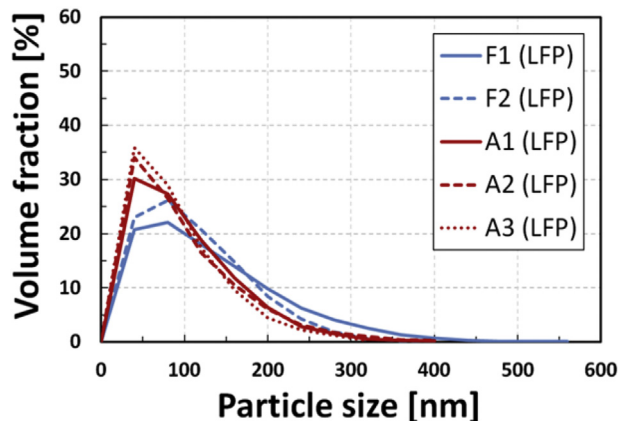


Fig. 4. Particle size distribution for LFP.

visible near the edges of the LFP particles (Fig. 8a,b). The bright contrast near the edges of the LFP particle indicates a coating layer with a light atomic weight relative to the darker LFP core. High resolution images (Fig. 8c,d) reveal contrast details of the coating layer on the LFP particle at an atomic level:

1. A thin layer carbon coating layer with average thickness of 2–4 nm (labeled as (1) in Fig. 8c,d). This layer has the same thickness as that observed in the fresh sample, as shown in Fig. 7d, and is most likely the carbon coating already present in the commercial LFP powder.
2. A dark layer, labeled as (2) in Fig. 8 (c,d), with thickness of 10–15 nm. It appears darker than the first one which indicates that it is composed by heavier elements.
3. A bright layer (3) with a thickness of 20–25 nm.
4. A dark layer (4) with a thickness of 2–4 nm.

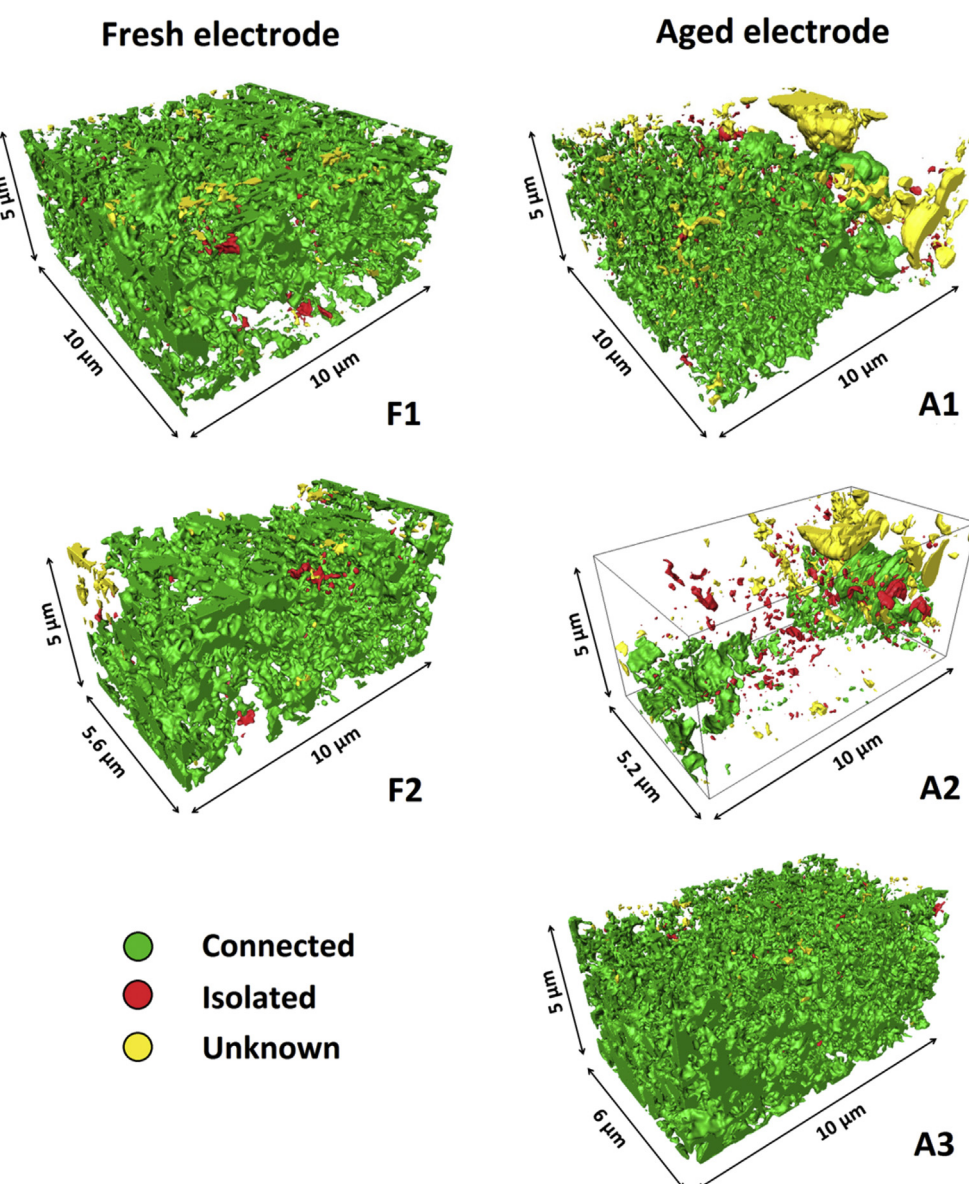


Fig. 5. Connectivity analysis of CB in the five 3D data sets. Green particles are connected with the bottom of the segmented volume (closest to the aluminum current collector). Red particles are unconnected and yellow particles are unknown (could be connected outside the segmented volume).

Table 4

Connectivity volume fraction for fresh and aged electrode.

Connectivity	F1	F2	Fresh (av. and deviation)	A1	A2	A3	Aged (av. and deviation)
Connected	97%	97%	97% ± 0%	78%	64%	98%	80% ± 14%
Isolated	2%	2%	2% ± 0%	5%	16%	1%	7% ± 6%
Unknown	1%	1%	1% ± 0%	17%	20%	1%	13% ± 8%

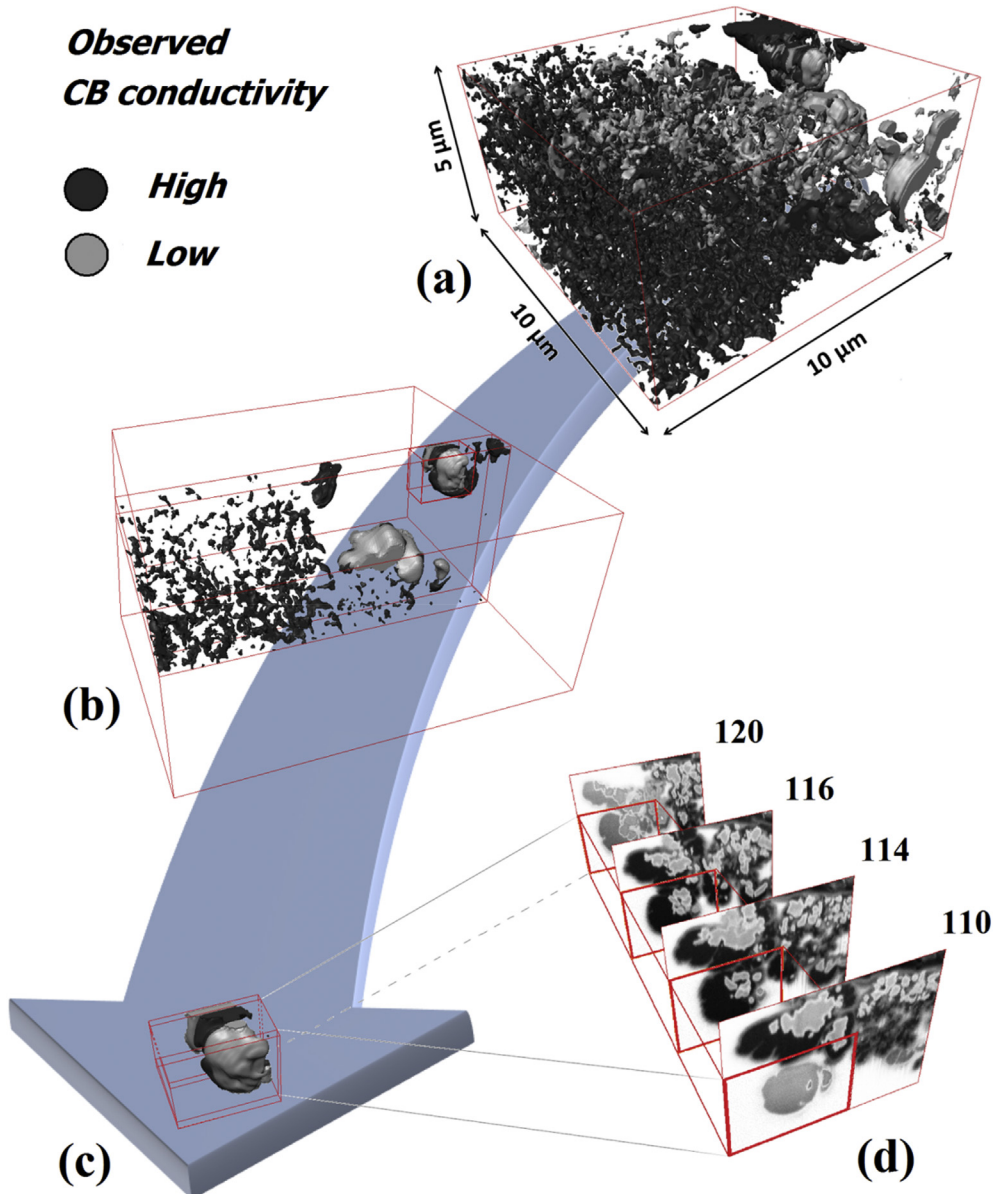


Fig. 6. a) Segmentation of apparently percolated (black) and non-percolated (gray) CB from a 3D FIB tomography reconstruction of sample A1 based on SEM images recorded with an In-lens detector at 1 kV b) and c) shows a zoom on a smaller section of the volume and d) examples of slices (raw SEM images) in the 3D dataset. Slice numbers are indicated in the figure.

Table 5

Observed high- and low-conductivity in the fresh and aged electrode samples.

Observed CB conductivity	F1	F2	Fresh (av. and deviation)	A1	A2	A3	Aged (av. and deviation)
High	100%	100%	100% ± 0%	75%	71%	100%	82% ± 13%
Low	0%	0%	0% ± 0%	25%	29%	0%	18% ± 13%

HRTEM imaging combining with Fourier transform deduced

from HRTEM images indicates that the LFP particle cores preserve

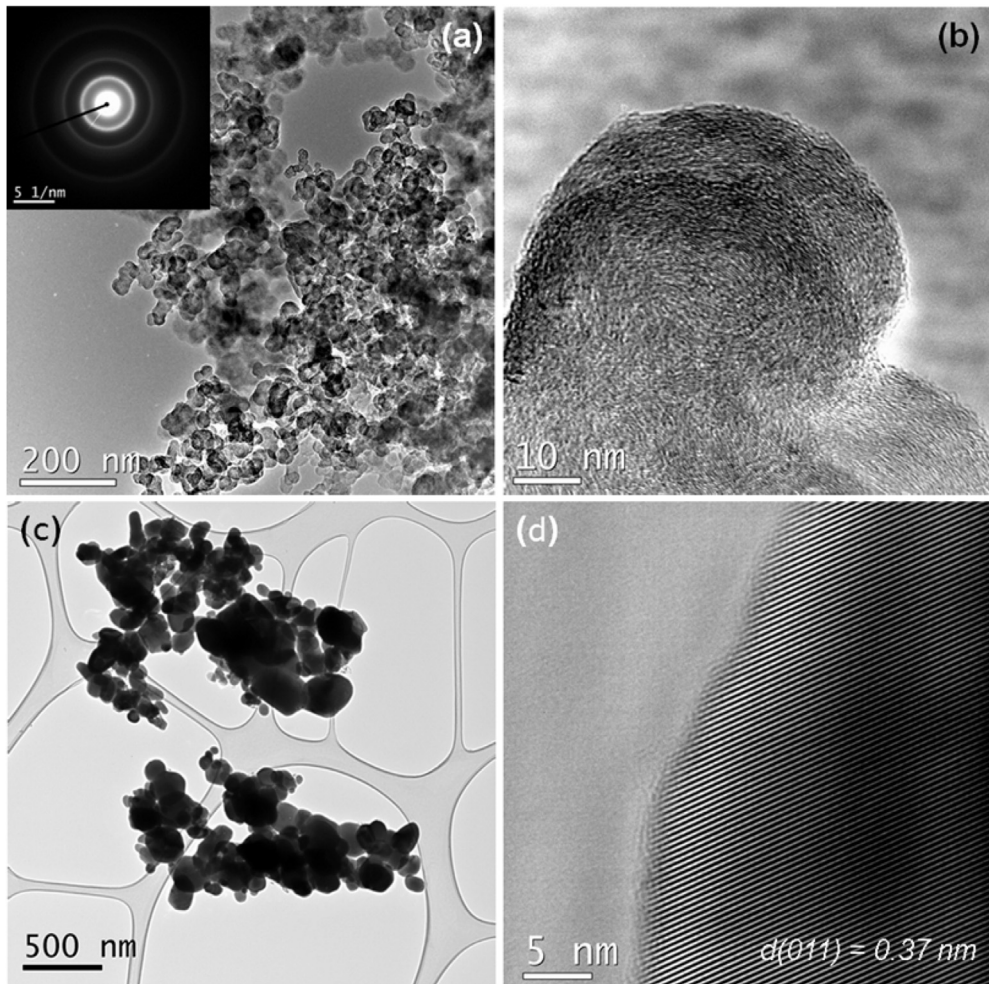


Fig. 7. (a) TEM image of fresh CB. The inset shows SAED pattern from the corresponding area. (b) HRTEM image of fresh CB nanoparticles indicating quasi-crystalline structure of graphene sheets in the particles. (c) TEM image of LFP nanoparticles on lacey carbon film, and (d) HRTEM image of a LFP nanoparticle with contrast from (011) lattice planes ($d = 0.37 \text{ nm}$) and with a thin coating layer.

their crystalline structure (orthorhombic structure) denoted by crystal planes visible in Fig. 8d whereas the coating layer on the LFP particles are amorphous.

4. Discussion

4.1. Morphological changes

PSD calculation of LFP and connectivity analysis of CB has been used to study morphological degradation in a LFP/CB electrode. The LFP PSD in Fig. 4 shows a slight shift towards smaller grains in the aged samples compared to the fresh samples, probably due to cracking of the particles (Fig. 2 e,f). This creates new secondary smaller particles which are not connected or poorly connected to the carbon black network. Due to low ionic and electronic conduction of LFP, the cracks will likely cause parts of the old particles and some of the new LFP particles formed by cracking to become electrochemically inactive such that they cannot participate in the overall (de)lithiation reaction in the electrode, resulting in a drop in electrode capacity. Furthermore, olivine LiMPO₄ (with M = Fe, Mn, Co) in presence of HF, developed by LiPF₆ electrolyte decomposition, are known to be subjected to M dissolution, which leads to capacity fading [33,34]. This process is usually accelerated if the active material is not protected by a carbon coating [34], thus the

particle cracking observed by PSD distribution (Fig. 4) and SEM images at 10 kV (Fig. 2 e,f) suggests that the increased surface area of non-carbon coated LFP accelerates the iron dissolution.

Regions A1 and A2 are characterized by the worst CB connectivity to the current collector (Fig. 5 and Table 4), because of relatively big carbon agglomerates disconnected from the CB network. On the other hand, no significant changes are observed between A3 and the fresh electrode. This suggests that CB degradation occurs heterogeneously throughout the sample and that carbon particles probably tend to agglomerate with cycling, reducing the electron supply needed for LFP (de)lithiation. Zhu et al. [9] showed that CB additive tends to aggregate and attach on the active material surface (n.b. LFP), especially with a high CB/LFP mass ratio as in our cathodes (10%:80%). However the continuous CB agglomeration on LFP surface upon cycling could be an effect of two different kind of degradation:

1. Mechanical stress, due to expansion/contraction of LFP during charging/discharging cycling, which would cause CB attachment on LFP surface and detachment from other sites;
2. Iron dissolution [34]. It is believed that this process causes the loss of contact between active materials (LFP) and conductive CB [34] with consequent agglomeration on other LFP grains.

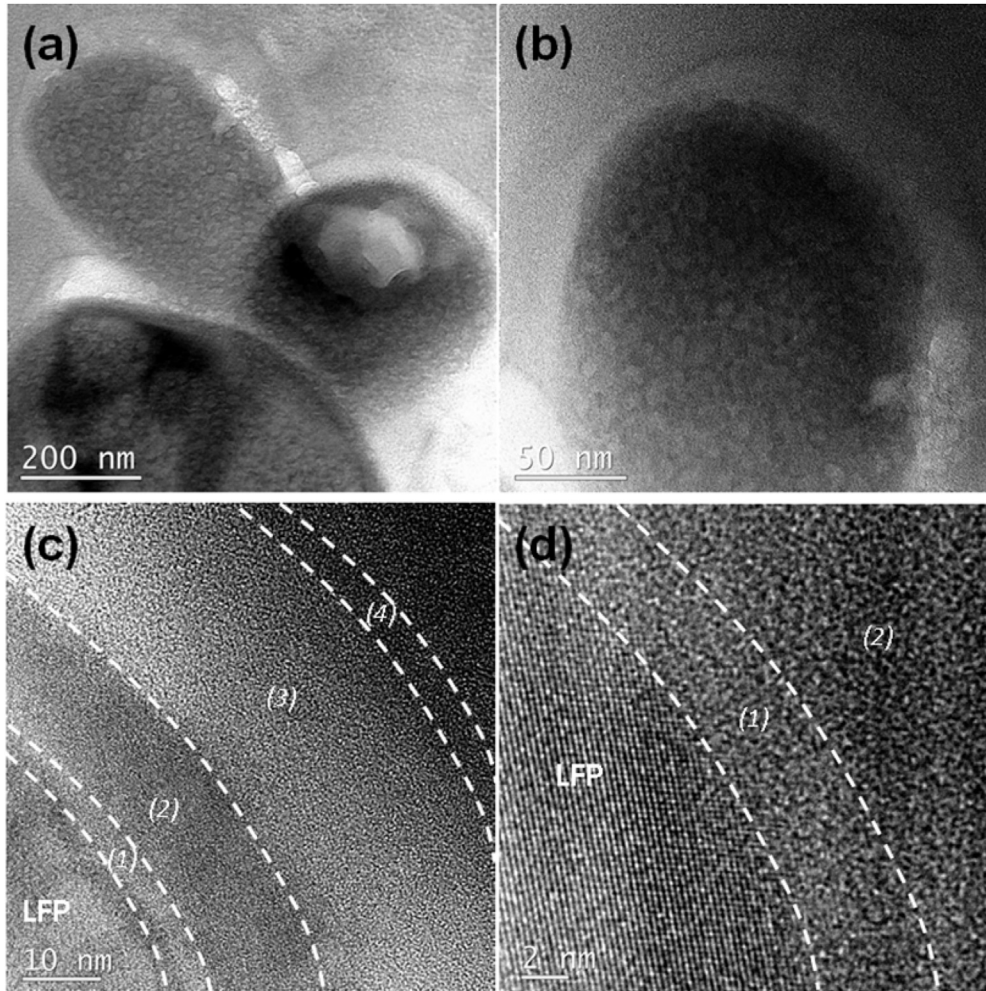


Fig. 8. (a, b) TEM images of LFP/CB aged cathode, (c, d) HRTEM images of the edge of the LFP particle presented in (b).

4.2. Charge contrast

Morphological changes are not the only degradation mechanism observed with cycling. Another important aspect is the observed change in the electronic conductivity of the CB agglomerates. Charge contrast FIB/SEM tomography was used to resolve high- and low-conductivity CB. The fresh electrode is characterized by high-conductivity CB, whereas localized charging is observed in the aged samples, A1 and A2. A3 does not show any charging phenomena, confirming that degradation of the LFP/CB electrode occurs heterogeneously.

The reason for the low electronic bulk conductivity in the CB agglomerates is probably due to structural degradation. TEM images of a sample from the aged electrode show carbon surrounding the LFP particles that seems to be amorphous, in contrast to the quasi-crystalline fresh CB particles. The reason for the formation of the large amorphous structures in the degraded electrode is currently not known by the authors. A possible reason for structural changes of CB during charge/discharge cycling could be its dissolution and subsequent agglomeration in the amorphous form at other sites in the electrode [35]. The change from a quasi-crystalline structure to an amorphous structure is known to decrease the electronic conductivity [19,20] several orders of magnitude [36,37]. It is reported in literature that the electrical resistivity of crystalline graphite is around $10^{-5} - 10^{-3}$ Ωm , while in

bulk amorphous carbon is around $10^3 - 10^{13}$ Ωm [37].²

4.3. SEI-like layer

It is well known that the positive electrode materials are reactive with the most common electrolyte solutions, forming SEI phases at the interphase between salt-based and solvent-based species [38]. Specifically, the LiFePO₄ electrode material, in the presence of 1 M LiPF₆ in 1:1 EC:DMC electrolyte reacts, creating an SEI-like layer composed by different species, such as Li-organic species, Fluorophosphates and LiF [38]. This is likely what we observed in our LFP particles, as the first SEI layer denoted (2) in Fig. 8c,d possibly formed once the electrode has been soaked into the electrolyte. This layer can be distinguished from the first carbon layer because appears darker, being composed by heavier element such as F, P, O coming from electrolyte decomposition.

As discussed above, cycling the battery for 100 cycles, causes carbon agglomeration on the LFP surface, it could therefore be suggested that the 3rd relatively thick and bright layer, denoted (3) in Fig. 8c, is the initiation of the carbon agglomeration. This carbon layer appears amorphous in contrast to the crystallinity of the fresh Super C65 structure. If the original CB particles, with degradation,

² A video showing rotations of the 3D structures is available as supplementary material.

dissolves and agglomerate as amorphous structures on LFP surfaces, this could partly explain the reduced the electrical conductivity and decreased cathode performance. It can be speculated that the 4th relatively thin and dark layer in Fig. 8c is an SEI-like layer which deposited after the battery cycling was ended. It should, however be emphasized that further characterization is needed to verify the composition of the amorphous layers.

5. Conclusions

In this work a fresh and a degraded laboratory-made Li-ion battery LFP/CB cathode were characterized by SEM, TEM and low-kV FIB/SEM analysis. Five samples, two from the fresh cathode and three from the degraded cathode were analyzed.

Lateral E-T detector imaging provided brightness contrast between LFP, CB and pores, which allowed phase separation and segmentation of the electrode samples.

LFP particle size distribution analysis revealed that the aged cathode had a higher amount of smaller LFP particles than the amount observed in the fresh electrode, probably due to cracking of the LFP particles during cycling. This was supported by the observation of visible cracks in the bigger LFP particles in the degraded electrode using 10 kV SEM imaging.

The CB particles were seen to agglomerate and accumulate on the LFP surface in some parts of the aged electrode, increasing heterogeneity of the CB network and reducing electron percolation thereby decreasing the amount of electrochemically active LFP particles.

Low accelerating voltage (1 kV) permitted a detailed study of charging effects in CB agglomerates observed in the aged cathode. The interpretation of low-kV SEM imaging, that charging effects correlate with electronic percolation, was shown to be incomplete in the analysis of the CB agglomerates. A careful analysis of the 3D low-kV images indicated that the CB agglomerates do not have a sufficient bulk electronic conductivity to dissipate the electrons induced by the SEM imaging. However, the CB/vacuum interface seems to have sufficient conductivity to dissipate the electrons induced by the SEM imaging. In conclusion the low-kV SEM in-lens imaging can provide a useful contrast between high-conductivity carbon phases and low-conductivity carbon phases with no electronic percolation to high-conductivity carbon phases at the carbon/vacuum interface. We can observe from the contrast difference that the CB is moving toward lower conductivity, indicating the presence of a different structure as later confirmed by TEM analysis. The poor electronic conductivity of the CB agglomerates is attributed to a change in the structure from quasi-crystalline to amorphous, supported by HRTEM analysis of the degraded cathode, which would increase the electrical resistivity of carbon from 10^{-5} – 10^{-3} Ωm to around 10^3 – 10^{13} Ωm [37].

The presented method combining low-kV SEM in-lens imaging with FIB 3D tomography can yield detailed information about the amount of low-conductivity carbon in aged LFP/CB electrodes and we hope the method will prove valuable in failure analysis of battery electrodes, thereby assisting in improving existing and future battery technologies.

Acknowledgments

The authors gratefully acknowledge financial support from the Danish strategic research council through the project “Advanced Lifetime Prediction of Battery Energy Storage” (contract no. 0603-00589B). The authors wish to thank Ebtisam Abdellahi for laboratory assistance and sample preparation. The authors at Northwestern gratefully acknowledge the financial support from the Office of Naval Research Grant #N00014-12-1-0713.

References

- [1] M. Armand, J.M. Tarascon, *Nature* 451 (2008) 652–657.
- [2] B. Scrosati, J. Hassoun, Y.K. Sun, *Energy Environ. Sci.* 4 (2011) 3287–3295.
- [3] J.M. Tarascon, M. Armand, *Nature* 414 (2001) 359–367.
- [4] A.K. Padhi, K.S. Nanjundaswamy, J.B. Goodenough, *J. Electrochem. Soc.* 144 (1997) 1188–1194.
- [5] Y. Wang, P. He, H. Zhou, *Energy Environ. Sci.* 4 (2010) 805–817.
- [6] H. Gabrisch, J. Wilcox, M.M. Doeff, *Electrochem. Solid-State Lett.* 11 (2008) A25–A29.
- [7] H.Y.S. Huang, Y.X. Wang, *J. Electrochem. Soc.* 159 (2012) A815–A821.
- [8] D. Wang, X. Wu, Z. Wang, L. Chen, *J. Power Sources* 140 (2005) 125–128.
- [9] M. Zhu, J. Park, A.M. Sastry, *J. Electrochem. Soc.* 158 (2011) A1155–A1159.
- [10] X. Qi, B. Blizanac, A. DuPasquier, M. Oljaca, J. Li, M. Winter, *Carbon* 64 (2013) 334–340.
- [11] J.R. Wilson, W. Kobsiriphat, R. Mendoza, H.Y. Chen, J.M. Hiller, D.J. Miller, K. Thornton, P.W. Voorhees, S.B. Adler, S.A. Barnett, *Nat. Mater.* 5 (2006) 541–544.
- [12] T. Hutzenlaub, S. Thiele, R. Zengerle, C. Ziegler, *Electrochem. Solid-State Lett.* 15 (2012) A33–A36.
- [13] M. Ender, J. Joos, T. Carraro, E. Ivers-Tiffée, *J. Electrochem. Soc.* 159 (2012) A972–A980.
- [14] Z. Liu, J.S. Cronin, Y.K. Chen-Wieart, J.R. Wilson, K.J. Yakal-Kremski, J. Wang, K.T. Faber, S.A. Barnett, *J. Power Sources* 227 (2013) 267–274.
- [15] M. Ender, J. Joos, T. Carraro, E. Ivers-Tiffée, *Electrochem. Commun.* 13 (2011) 166–168.
- [16] J.S. Cronin, J.R. Wilson, S.A. Barnett, *J. Power Sources* 196 (2011) 2640–2643.
- [17] J.S. Cronin, Y.K. Chen-Wieart, J. Wang, S.A. Barnett, *J. Power Sources* 233 (2013) 174–179.
- [18] K. Thydén, Y.L. Liu, J.B. Bilde-Sørensen, *Solid State Ionics* 178 (2008) 1984–1989.
- [19] M.M. Doeff, J.D. Wilcox, R. Kostecki, G. Lau, *J. Power Sources* 163 (2006) 180–184.
- [20] R. Kostecki, B. Schnyder, D. Alliata, X. Song, K. Kinoshita, R. Kötz, *Thin Solid Films* 396 (2001) 36–43.
- [21] M.T. Postek, *Rev. Sci. Instrum.* 61 (1990) 3750.
- [22] J. Cazaux, *J. Microsc.* 214 (2004) 341–347.
- [23] J. Cazaux, *J. Phys. D. Appl. Phys.* 38 (2005) 2433–2441.
- [24] K. Kumagai, T. Sekiguchi, *Ultramicroscopy* 109 (2009) 368–372.
- [25] J. Cazaux, *Micron. Microanal.* 10 (2004) 670–684.
- [26] D.J. Stokes, *Philos. Trans. R. Soc. Lond. A* 361 (2003) 2771–2787.
- [27] W. Li, W. Bauhofer, *Carbon* 49 (2011) 3891–3898.
- [28] D.C. Joy, *Scanning* 17 (1995) 270. Data available at: <http://web.utk.edu/~srcutk/htm/interact.htm>.
- [29] P. Hovington, D. Drouin, R. Gauvin, D.C. Joy, N. Evans, *Scanning* 19 (1997) 29–35.
- [30] J. Sauvola, M. Pietikäinen, *Pattern Recognit.* 33 (2000) 225–236.
- [31] T. Kryjak, M. Gorgoń, *Int. J. Appl. Math. Comput. Sci.* 20 (2010) 571–580.
- [32] B. Münch, L. Holzer, *J. Am. Ceram. Soc.* 91 (2008) 4059–4067.
- [33] B.S.M. Oh, S.W. Oh, C.S. Yoon, B. Scrosati, K. Amine, Y.K. Sun, *Adv. Funct. Mater.* 20 (2010) 3260–3265.
- [34] X. Zhi, G. Liang, L. Wang, X. Ou, J. Zhang, J. Cui, *J. Power Sources* 189 (2009) 779–782.
- [35] M. Kerlau, M. Marcinek, R. Kostecki, *J. Power Sources* 174 (2007) 1046–1051.
- [36] M.M. Doeff, Y. Hu, F. McLarnon, R. Kostecki, *Electrochem. Solid-State Lett.* 6 (2003) A207–A209.
- [37] K. Saito, J. Fujii, T. Kizuka, *Jpn. J. Appl. Phys.* 48 (2009) 010218.
- [38] M. Cuisinier, N. Dupré, J.F. Martin, R. Kanno, D. Guyomard, *J. Power Sources* 224 (2013) 50–58.